Nuclear Engineering and Technology 59 (2027) 104837

Contents lists available at ScienceDirect

Nuclear Engineering and Technology

journal homepage: www.elsevier.com/locate/net

Original Article

A simple and practical correction procedure for non-uniformity in quantitative X-ray images generated with an energy-resolving photon-counting detector

Hiroaki Hayashi [a,*], Rina Nishigami [b], Daiki Kobayashi [b], Takuya Kasue [b], Mana Mitani [b], Lisa Yakushiji [c], Natsumi Kimoto [d], Takashi Asahara [e]

[a] College of Transdisciplinary Sciences for Innovation, Kanazawa University, Kakuma-machi, Kanazawa, Ishikawa, 920-1192, Japan
[b] Graduate School of Medical Sciences, Kanazawa University, 5-11-80, Kodatsuno, Kanazawa, Ishikawa, 920-0942, Japan
[c] School of Health Sciences, College of Medical, Pharmaceutical and Health Sciences, Kanazawa University, 5-11-80, Kodatsuno, Kanazawa, Ishikawa, 920-0942, Japan
[d] Department of Radiological Science, Faculty of Health Sciences, Junshin Gakuen University, 1-1-1 Chikushigaoka, Minami-Ku, Fukuoka, 815-8510, Japan
[e] Department of Radiological Technology, Faculty of Health Sciences, Okayama University, 2-5-1 Shikata-cho, Kita-Ku, Okayama, 700-8558, Japan

ARTICLE INFO

Keywords:
X-ray non-destructive test
Photon-counting detector
Quantitative images
Non-uniform image artifacts

ABSTRACT

This study proposes a simple procedure for correcting non-uniform image artifacts in quantitative X-ray imaging using energy-resolving photon-counting detectors (ERPCDs) during non-destructive testing. Attenuation values $(\mu t)_l$ and $(\mu t)_h$ from low- and high-energy bins were modified using correction coefficients α & β. First, to determine these coefficients, five carbon–aluminum combination phantoms were imaged, and effective atomic number (Z_{eff}) and effective mass thickness ($\rho_{eff}t$) images were calculated for all patterns in which α & β were varied within the range of 0.90–1.10. Next, permissible regions were defined in the α-β coordinate plane where deviations from theoretical values were ≤2% for Z_{eff} and ≤5% for $\rho_{eff}t$. Then, for the regions where the two permissible regions overlap, the pair {α*, β*} which is the closest to {1, 1} was derived. These suitable pairs were calculated for each Z_{eff} sample, and the correction coefficient functions of $\alpha(Z_{eff})$ & $\beta(Z_{eff})$ were calculated for each image column. These correction functions were incorporated into the quantitative image calculation algorithm. As a result, our procedure reduced root-mean-square error by 78%–88% for Z_{eff} images and 18%–68% for $\rho_{eff}t$ images. Furthermore, we demonstrated the effectiveness and feasibility of the proposed procedure using actual food samples.

1. Introduction

Non-destructive testing (NDT) using X-rays is widely employed across a range of fields from food products to industrial goods, and thereby safeguards our quality of life [1,2]. Generally, foreign objects in X-ray inspections have been identified by observing the shadow image produced by X-rays [3]. However, this approach relied heavily on the limitation that current image detectors could only generate one-dimensional grayscale image density information. Currently, energy-resolving photon-counting detectors (ERPCDs) have been developed and this enables quantitative imaging that utilizes the energy information of each X-ray [4,5]. For example, it has been reported that effective atomic number (Z_{eff}) images [6–9], effective density (ρ_{eff}) images [10,11], bone enhanced high-contrast images [12], and soft-tissue/bone extraction images [13] can be generated.

Extensive research has been conducted on ERPCD-type computed tomography (CT) for medical applications [14–17], and results based on clinical images have been reported [5]. Since these studies utilized manufacturer-calculated virtual monoenergetic images (VMIs), in which the various corrections relevant to the present study had already been applied, researchers were able to focus on algorithm development and/or clinical research [7,8]. On the other hand, for ERPCDs intended for NDTs, the users must perform corrections related to pixel differences, because variations between pixels are not corrected and artifacts related to the differences are clearly presented.

* Corresponding author.
E-mail addresses: hayashi.hiroaki@staff.kanazawa-u.ac.jp (H. Hayashi), nishigami.rina@gmail.com (R. Nishigami), kobayashi.daiki.2022@gmail.com (D. Kobayashi), takuya.kasue.1120@gmail.com (T. Kasue), m-mitani12@s.okayama-u.ac.jp (M. Mitani), lisa.yakushiji.0814@gmail.com (L. Yakushiji), natsumi.kimoto.0717@gmail.com (N. Kimoto), takashi.asahara.111@gmail.com (T. Asahara).

https://doi.org/10.1016/j.net.2026.104837
Received 25 August 2026; Received in revised form 8 October 2026; Accepted 6 November 2026
Available online 6 November 2026
1738-5733/© 2026 Korean Nuclear Society, Published by Elsevier Korea LLC. This is an open access article under the CC BY license (http://creativecommons.org/licenses/by/4.0/).

Abbreviations:

NDT	Non-destructive testing
ERPCD	Energy resolving photon-counting detector
ACM	Anti-coincidence mode
TDI	Time delay integration
Z_{eff}	Effective atomic number
ρ_{eff} t	Effective mass thickness
RMSE	Root mean square error

One of the challenges in using ERPCD is that the sensor output varies from pixel to pixel, resulting in image non-uniformity. As shown in Fig. 1, image non-uniformity arises from variations in the X-ray-receiving area among pixels, as well as differences in X-ray energy threshold settings (ΔE_l and ΔE_h) and detector response characteristics ($\mathbf{R}^{(1,2)} = \mathbf{R}^{(1)} \times \mathbf{R}^{(2)}$), in which $\mathbf{R}^{(1)}$ is response characteristics of radiation transportation and $\mathbf{R}^{(2)}$ is that of charge sharing effect [18]. Taking the big picture into account, the differences between sensor units are a major factor, and it is surmised that the parameters vary either by sensor unit or at the finer pixel level. In Fig. 1, settings for unit 1 are described as $\Delta E_{l,1}$, $\Delta E_{h,1}$, and $\mathbf{R}_1^{(1,2)}$. Since the parameters are different for each detection instrument, it is preferable to apply corrections to the actually acquired data using a practical software approach. When performing inspections using conventional gray-scale images, this issue can be resolved by applying a correction factor to calibrate the measured image so that pixel brightness is uniform across the entire image. In the case of using the calibration phantom, correction may be applied to ensure the phantom image is displayed uniformly [19–21]. In these cases, the visibility of the generated image has taken precedence. However, when calculating quantitative images using ERPCDs, deeper correction is required because the corrected values must reflect the accurate amount of X-ray attenuation [6].

There are very few studies investigating the relationship between image non-uniformity and material identification performance. Naidu et al. conducted pioneering work on evaluating material decomposition accuracy and proposed a model to correct for inhomogeneity when imaging various materials via X-ray CT [22]; their approach involves estimating ideal signal intensities and applying corrections to match those responses. In contrast, our approach provides a simple correction procedure for NDT systems using two-dimensional X-ray projection images. For the NDT application, computational speed is prioritized; therefore, a simple and computationally efficient correction procedure is desirable. Our procedure proposed in this paper is very simple and resolves the issue of image non-uniformity using only two correction coefficients.

The objective of this study is to propose a simple and practical correction procedure that prevents non-uniform image artifacts when quantitative images are generated using ERPCDs, and to demonstrate our procedure using an actual NDT system. Our correction procedure aims to ensure that the values represented in quantitative images are highly accurate without including significant systematic uncertainties. Our procedure corrects the inaccuracies in the raw data used for image generation, rather than modifying the specific images. Consequently, issues regarding heterogeneity in any quantitative images derived from the same raw data are resolved simultaneously. This is not simply about modifying pixel values to improve inspection procedures that utilize visual information, but rather about providing a technology that will serve as the foundation for the development of new inspection methods based on quantitative analysis.

2. Materials and methods

2.1. Concept of correction procedure

Fig. 2 is a conceptual diagram of the data analysis flow for calculating quantitative images using ERPCDs. Quantitative image analysis involves using mathematical algorithms to analyze the X-ray attenuation value $\mu t = \ln(I_0/I)$, which is calculated with Lambert-Beer's law. Here, I_0 and I are the X-ray intensities in the absence of a subject and those in the presence of a subject, respectively. μ is the linear attenuation coefficient, and theoretically calculated data are usually provided as μ/ρ,

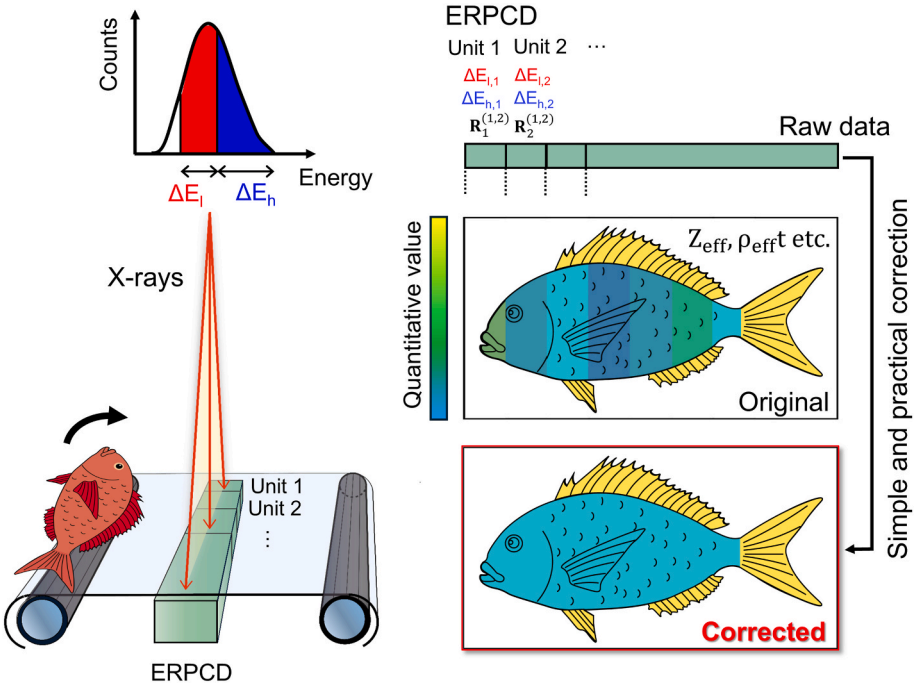

Fig. 1. A conceptual diagram illustrating the formation of non-uniform image artifacts in quantitative X-ray images generated using an ERPCD. The purpose of this study is to propose a practical simple correction procedure for generating uniform images when calculating quantitative images.

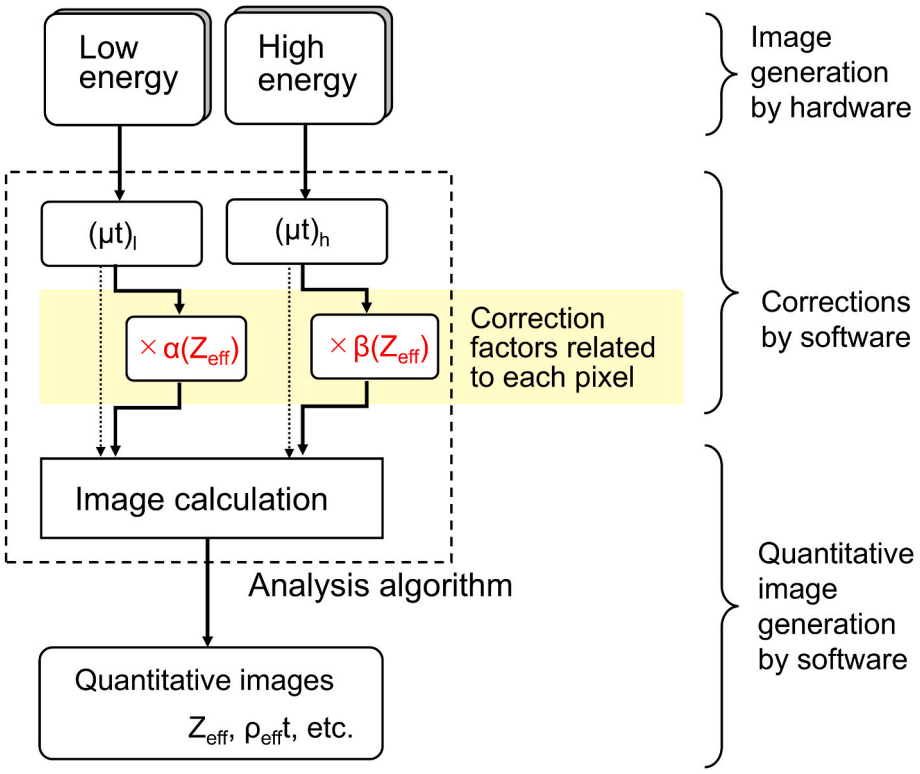

Fig. 2. Conceptual diagram of a practical correction procedure for measurement data μt using α & β.

which is called the mass attenuation coefficient [23].

Generally, non-uniformity in conventional images is corrected by applying a correction coefficient to measured count images; the factor is independently determined column-wise. For this correction process, the same correction coefficient is applied to the corresponding pixels of the I and I_0 images. However, when performing quantitative calculations based on X-ray attenuations, $\mu t = \ln(I_0/I)$ should be initially processed. In this case, since the correction factors applied to I and I_0 are identical, they cancel each other out during the calculation process. In other words, although conventional image non-uniformity correction improves the visibility of the conventional X-ray images, this correction is not reflected in the calculation process using μt values.

In this study, we propose a procedure to improve the non-uniformity of "quantitative images" by multiplying μt by a correction factor. Specifically, coefficients of α & β are defined as follows, and applied to the X-ray attenuation values ($(\mu t)_l$ and $(\mu t)_h$) obtained in the low- and high-energy bins. This correction can intentionally modify the experimentally measured attenuation values.

$$\text{Low energy} : \alpha \times (\mu t)_l \tag{1-1}$$

$$\text{High energy} : \beta \times (\mu t)_h \tag{1-2}$$

The correction factors α & β should be applied to the μt values. This is because the most fundamental physical quantity measured by ERPCDs is μt value [8,12,13], and various quantitative images can be additionally derived through calculations based on these values. Correcting the μt values to their true values can simultaneously resolve issues regarding non-uniform image artifacts across the various quantitative images that are calculated based on the μt values. In this modification process, α & β are not constants but are assumed to be "functions" that depend on the effective atomic number of the object. Therefore, in this paper, we defined the correction coefficients as functions in the manner described below. Defining the correction coefficients as functions of Z_{eff} represents a key feature of this study.

$$\alpha \rightarrow \alpha(Z_{eff}) \tag{2-1}$$

$$\beta \rightarrow \beta(Z_{eff}) \tag{2-2}$$

This paper presents procedures for determining α & β, and reports the results of demonstration experiments using NDT equipment. Because images were generated using time delay integration (TDI) mode, the correction coefficients were determined independently for each detector column.

2.2. *Quantitative image analysis algorithm incorporating α & β correction*

A feature of this study is the application of Z_{eff}-dependent correction factors. However, at the beginning of the quantitative value analysis based on μt values, the subject's Z_{eff} is not determined. In other words, it is necessary to apply a correction factor to μt values without using the information of a finally determined Z_{eff} value. The fundamental aspect of this problem is shared with the process of calculating the Z_{eff} value; a beam-hardening correction, which strongly corresponds to Z_{eff} values, should be performed to μt values at the initial stage of the quantitative image calculation. Therefore, we attempt to resolve the issue by incorporating newly proposed correction factors into the Z_{eff} calculation algorithm which was proposed by Kimoto et al. [6].

Fig. 3 shows the data workflow of the quantitative image analysis algorithm for calculating Z_{eff} and effective mass thickness ($\rho_{eff}t$), which was modified to incorporate α & β corrections. The physical quantities obtained from the initial measurements by ERPCD are $(\mu t)_{l,meas}$ and $(\mu t)_{h,meas}$. Since $(\mu t)_{l,meas}$ and $(\mu t)_{h,meas}$ were affected by the effects of beam hardening (BH) and detector response (DR), and therefore these effects were corrected by the procedure proposed by our group [6,24]. Then, the corrected value of $(\mu t)_{l,cor}$ and $(\mu t)_{h,cor}$ can be derived. Furthermore, by applying the corrections for α & β proposed in this paper, the correct attenuation values are calculated, and these values serve as input data for the Z_{eff} and $\rho_{eff}t$ calculation algorithms [6,10].

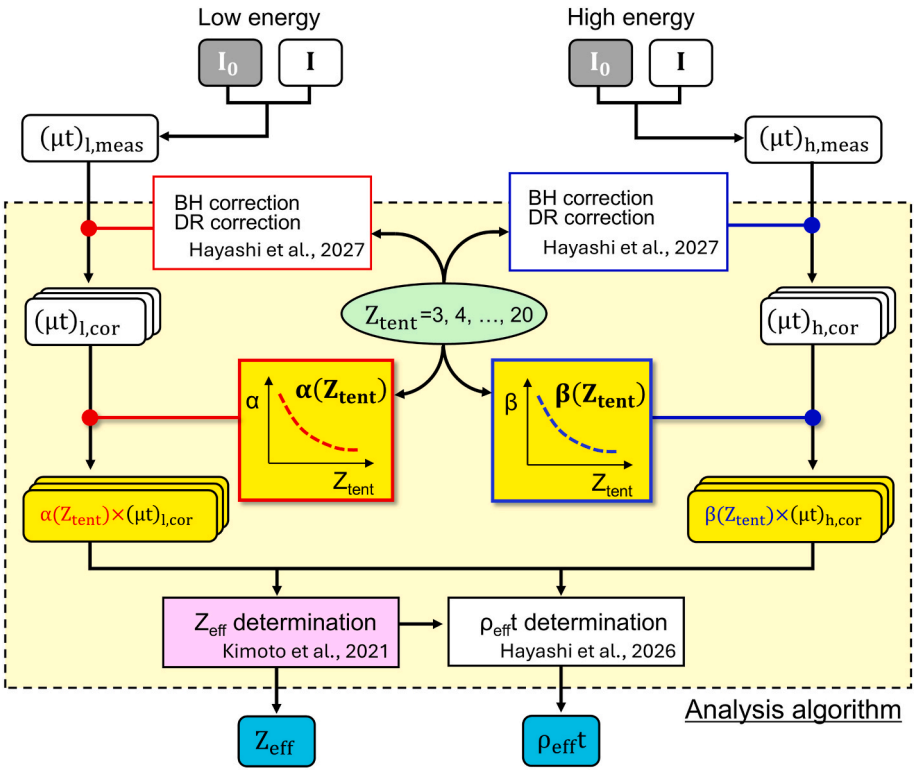

Fig. 3. Data analysis workflow of a quantitative image analysis algorithm, in which a correction related to α & β is incorporated.

This sequence of data flows is shown in Fig. 3, but it can be briefly summarized as follows:

$$(\mu t)_{l,meas} \xrightarrow[\text{DR correction}]{\text{BH correction}} (\mu t)_{l,cor} \xrightarrow{\alpha\ \text{correction}} \alpha(Z_{tent}) \times (\mu t)_{l,cor}, \quad (3\text{-}1)$$

$$(\mu t)_{h,meas} \xrightarrow[\text{DR correction}]{\text{BH correction}} (\mu t)_{h,cor} \xrightarrow{\beta\ \text{correction}} \beta(Z_{tent}) \times (\mu t)_{h,cor}. \quad (3\text{-}2)$$

A feature of the algorithm shown in Fig. 3 is the use of tentatively estimated Z_{eff} values (Z_{tent}). Physical phenomena such as beam hardening effect, detector response characteristics, and corrections involving α & β depend on the effective energy of the X-ray spectrum. Consequently, they are indirectly influenced by the object's Z_{eff} value. However, since the Z_{eff} value is a result derived by the algorithm, the final Z_{eff} value cannot be used during the algorithm's initial stages. Therefore, the algorithm is executed while performing various corrections using Z_{tent}, and then the Z_{eff} value is ultimately determined.

Fig. 4 illustrates the relationship between Z_{tent} and the finally determined Z_{eff} value. Z_{tent} values with natural numbers such as 3, 4, …,

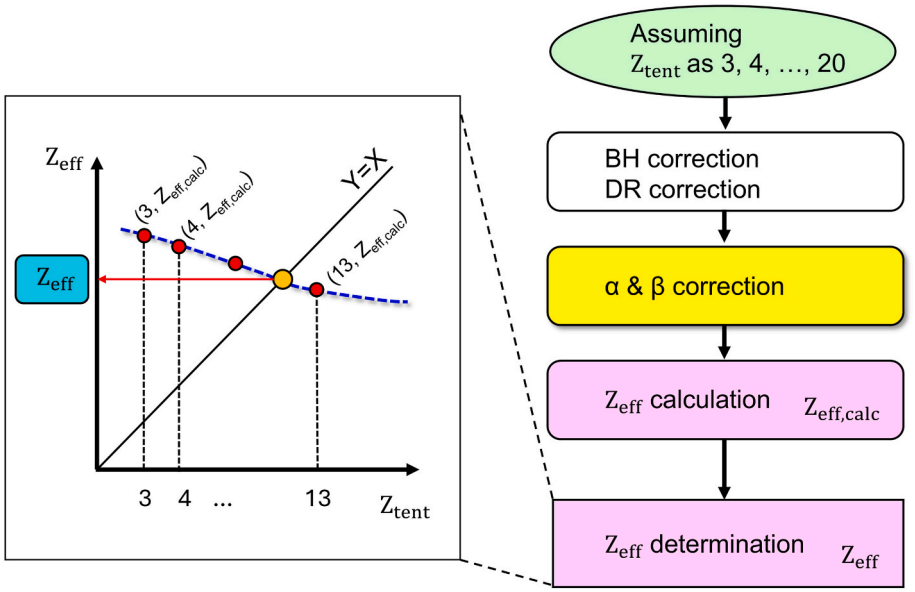

Fig. 4. Relationship between Z_{tent} and Z_{eff} used for various corrections. As shown in the graph on the left, in the final stage of the algorithm, the value satisfying $Z_{tent} = Z_{eff}$ is found to determine Z_{eff}.

13, …, and 20 are assumed. The algorithm is executed for each Z_{tent}. The first correction is the BH correction and DR correction, in which Z_{tent} is required. Next, by applying the α & β correction, modified attenuation values are calculated, in which the same Z_{tent} is used. Then, based on these values, the Z_{eff} value is calculated; this calculated Z_{eff} is denoted as $Z_{eff,\ calc}$:

$$Z_{eff,calc} = f\left(\frac{\beta(Z_{tent}) \times (\mu t)_{h,cor}}{\alpha(Z_{tent}) \times (\mu t)_{l,cor}}\right), \quad (4)$$

where f is a function for converting to the Z_{eff} from the ratio of $(\mu t)_h$ to $(\mu t)_l$ [6,24]. Since $Z_{eff,\ calc}$ value depends on Z_{tent}, a dataset of $\{Z_{tent}, Z_{eff,\ calc}\}$ is obtained by repeatedly performing $Z_{eff,\ calc}$ calculations for $Z_{tent} = 3, 4, \ldots$and 20. Finally, from this dataset, Z_{eff} can be determined by arithmetically identifying the data point of $Z_{tent} = Z_{eff}$ as shown in the left plot in Fig. 4.

2.3. Determination of α & β correction functions

2.3.1. Samples and experiments

To determine the correction functions for α & β, the bilayer samples shown in Fig. 5 [a] were measured. The samples are rods with five different Z_{eff} values. These samples were prepared by combining carbon rods with a density of 1.78 g/cm^3 (Toyo Tanso Co., Ltd., Osaka) and pure aluminum with a density of 2.70 g/cm^3. No. 1 consists of 16 mm of carbon; No. 2, 12 mm of carbon and 4 mm of aluminum; No. 3, 8 mm of carbon and 8 mm of aluminum; No. 4, 4 mm of carbon and 12 mm of aluminum; and No. 5, 16 mm of aluminum. The external dimensions of all phantoms were 378 mm (length) × 35 mm (width) × 16 mm (thickness). The reference values for Z_{eff} and $\rho_{eff}t$ for samples No. 1–5 were calculated by simulation calculation [25]. Then, the reference values for the physical constants of these rods were as follows: No. 1: $\{Z_{eff,ref}, \rho_{eff,ref}t\} = \{6.0, 2.85\ g/cm^2\}$, No. 2: {9.7, 3.25 g/cm^2}, No. 3: {11.3, 3.60 g/cm^2}, No. 4: {12.3, 3.96 g/cm^2}, and No. 5: {13.0, 4.32 g/cm^2}.

The imaging of the phantom was performed using an NDT system (System square Inc., Niigata, Japan). A typical layout of the system is provided in Ref. [24]. The imaging conditions were a tube voltage of 65 kV and a tube current of 2 mA. Under these conditions, the effect of pulse pile-up [26,27] was negligibly small. The X-ray tube utilizes an industrial X-ray imaging system (JOB CORPORATION, Kanagawa, Japan) equipped with a tungsten target. An aluminum plate with a thickness of 2.5 mm was installed as an inherent filter at the exit window of the X-ray tube. The distance from the X-ray focal spot to the ERPCD was 594 mm, and the sample was transported by a conveyor belt with a speed of 10 m/min. The distance between the X-ray detector and the sample was 32 mm.

The ERPCD employed a line sensor (TDI400.1.60.075.N, Varex Imaging Corporation, U.S.A.) utilizing a CdTe semiconductor (Acrorad Co., Ltd., Okinawa, Japan). The line sensor including 16 sensor units has outer dimensions of 410 mm × 6 mm, which consists of 4096 × 64 pixels, while we used 4096 × 60 pixels for image generation. The physical pixel size of the sensor was 100 × 100 μm^2. The physical density of CdTe was ρ = 5.85 g/cm^3, and the thickness was 0.75 mm [28]. The ERPCD settings consist of a low-energy bin of 35–45 keV and a high-energy bin of 45–65 keV. To reduce the effects of charge sharing, Anti-coincidence mode (ACM) was adopted, in which signals resulting from charge spreading during the X-ray absorption process are summed [29]. ACM is a hardware-based algorithm that performs coincidence counting of radiation signals within a cluster of adjacent 2 × 2 pixels and aggregates the summed energy information into the pixel with the highest signal value. Image reconstruction was performed using TDI mode. In this mode, counts are accumulated assuming a scan speed of 10 m/min, and the image is reconstructed via the shift-and-add method using information from 60 pixels that are aligned in the scan direction. The images were generated with a resolution of 4096 × 4096 pixels. Our system has a line rate of 1773 lines/s, and in this condition, the time required to generate a single image is 2.3 s. The subject image was binned 2 × 2 to reduce file size, and output from the device as a 2048 × 2048 pixel image.

The image data used for the analysis consisted of I_0 images acquired without the sample and I images acquired with the sample, with each set comprising images in both low-energy and high-energy bins. Namely, these four images constitute a single, independent dataset for a certain experiment. The I_0 images were acquired independently for all samples.

[a] Bilayer samples



Sample number	Thickness		$Z_{eff,ref}$	$\rho_{eff,ref}t$
	Carbon	Aluminum		
No. 1	16 mm	-	6.0	2.85 g/cm^2
No. 2	12 mm	4 mm	9.7	3.25 g/cm^2
No. 3	8 mm	8 mm	11.3	3.60 g/cm^2
No. 4	4 mm	12 mm	12.3	3.96 g/cm^2
No. 5	-	16 mm	13.0	4.32 g/cm^2

[b] Food samples



Fig. 5. Measured samples used in the experiment. [a] Bilayer samples used to generate the α & β functions; [b] food samples with various structures, intended to simulate non-destructive testing.

2.3.2. Analysis of α & β correction functions

This section describes the procedure for preparing the data used to construct the α & β correction functions. The images used are the bilayer samples No. 1–5 described in the previous section. Since the ground-truth values for Z_{eff} and $\rho_{eff}t$ are known for these images, the system can be calibrated to reproduce these correct values by selecting a suitable combination of α & β. The calculation of Z_{eff} [6] and $\rho_{eff}t$ [10] was performed using the algorithm proposed by our research group. Hayashi et al.'s algorithm calculates ρ_{eff} from CT data in which μ is imaged, but the exact same algorithm can be used to analyze data acquired by NDT equipment. Namely, in the case of NDT, μt (=μ×t) images are used as input data, so $\rho_{eff}t$ (=ρ_{eff}×t) can be calculated instead of ρ_{eff}. Fig. 6 illustrates the workflow for image data No. 3, and similar analyses were performed for No. 1 through No. 5.

First, the Z_{eff} image and $\rho_{eff}t$ image were calculated using a quantitative image algorithm. In this process, as shown in Figs. 2 and 3, Z_{eff} and $\rho_{eff}t$ images associated with a given α & β pair were calculated. In this process, α & β were varied in 0.01-step increments within the following range.

$$0.90 \le \alpha \le 1.10 \tag{5-1}$$

$$0.90 \le \beta \le 1.10 \tag{5-2}$$

Namely, there are 441 possible combinations of α & β within the range, and Z_{eff} and $\rho_{eff}t$ images were calculated for all of the patterns.

The α & β correction coefficients were calculated for each vertical line (i-th column) of the image. Then, for a given pair of {α, β}, we prepared a Z_{eff} image and a $\rho_{eff}t$ image as shown in Fig. 7 [step 1]. To perform simplified calculations, these images have been cropped to 2048 × 64 pixels. The mean values of the data in the i-th columns of the calculated images were determined, and the deviations Δ between the obtained values and the ground-truth values ($Z_{eff,ref}$ and $\rho_{eff,ref}t$) were calculated. They were then expressed as the absolute values of relative deviations, as shown in the following equation.

$$\mathrm{Diff}_Z = \frac{|\Delta Z_{eff}|}{Z_{eff,ref}} \tag{6-1}$$

$$\mathrm{Diff}_{\rho t} = \frac{|\Delta \rho_{eff}t|}{\rho_{eff,ref}t} \tag{6-2}$$

These values are calculated for a sample of a certain No., a pair of {α,β}, and for the i-th column.

The above operation shown in Fig. 7 [step 1] was performed for all pairs of {α, β} to calculate the corresponding "Diff_Z" and "$\mathrm{Diff}_{\rho t}$". Next, as shown in Fig. 7 [step 2], "Diff_Z" and "$\mathrm{Diff}_{\rho t}$" were plotted on the Z-axis against the plane of α (=X-axis) and β (=Y-axis). We need to find a suitable pair of {α, β} from this plot. The corrections performed in this paper are intended to practically compensate for error factors such as uncertainty in the detector settings. It is not assumed that both Z_{eff} and $\rho_{eff}t$ will reach perfectly optimal values through the application of α & β; suitable correction coefficients can only be obtained when both are in compromise with each other. Furthermore, since this correction should not excessively alter the original μt values, it is considered better to choose the {α, β} pair that is closer to {1, 1}, when similar results can be obtained. Therefore, the following α & β decision algorithm was constructed.

First, we set the permissible ranges for "Diff_Z" and "$\mathrm{Diff}_{\rho t}$" as follows:

$$\text{Permissible range for Z} : \mathrm{Diff}_Z \le 2\%, \tag{7-1}$$

$$\text{Permissible range for } \rho t : \mathrm{Diff}_{\rho t} \le 5\%. \tag{7-2}$$

For Z_{eff}, if it can be calculated with an uncertainty of around ±0.1, it would become a good imaging system [6]. The relative uncertainty for the Carbon sample is 0.1/6 = 0.016, so setting a tolerance of 2% is an appropriate target accuracy. Although there is no clear criterion for the target accuracy of $\rho_{eff}t$, we considered that a value of approximately ±0.05 g/cm^2 is appropriate for a typical mass thickness of 1.0 g/cm^3 × 1.0 cm = 1.0 g/cm^2, and set a tolerance of 5%.

Next, in the two-dimensional plots of α and β, pairs of {α, β} that fall within the "common" permissible range defined by equations (7-1) and (7-2) were extracted. The data points that minimize the following Euclidean distance between the reference point {α, β} = {1, 1} and the extracted {α, β} were determined. The determined suitable {α, β} pair

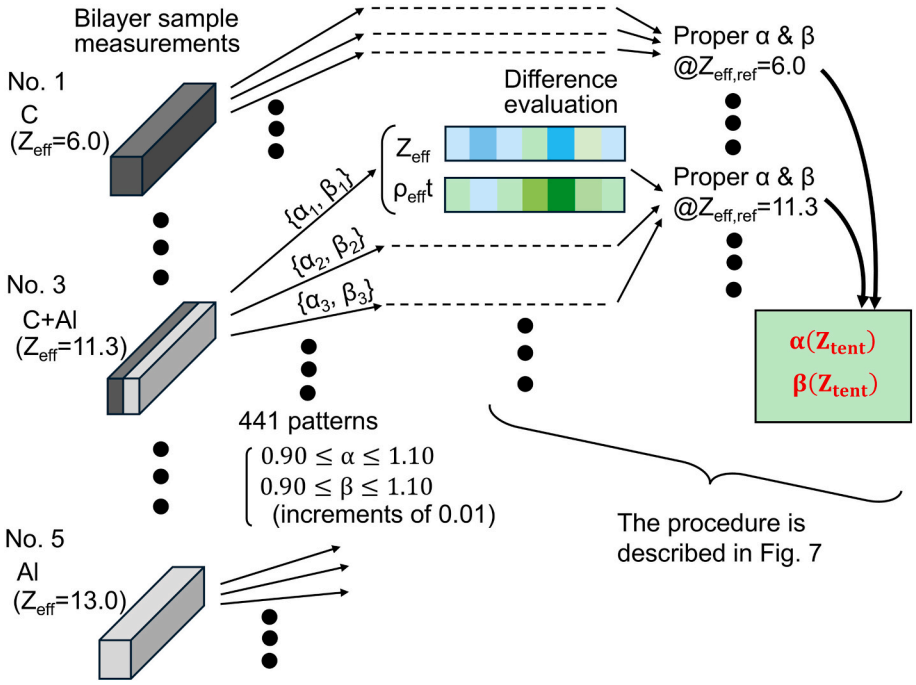

Fig. 6. Conceptual diagram of data analysis for determining α & β. For each sample, Z_{eff} and $\rho_{eff}t$ images were generated by intentionally varying α & β; these images were then analyzed to construct functions of α & β.

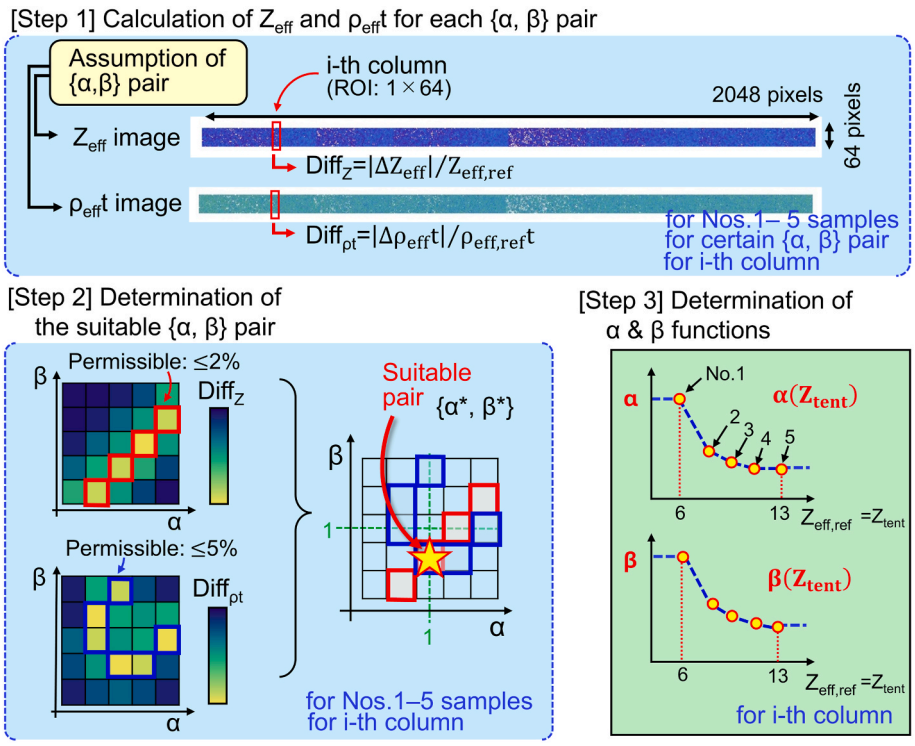

Fig. 7. Specific procedures for creating α & β functions. α & β functions were determined for each i-th column.

was defined as {α*, β*}.

$$\text{Suitable pair}: \{\alpha*, \beta*\} = \arg\ \min\sqrt{(\alpha_i - 1)^2 + (\beta_i - 1)^2} \tag{8}$$

Performing this operation calculates {α*, β*} for the i-th column of each sample number. Therefore, this series of operations is analyzed independently for all i and all sample numbers.

Finally, we will explain the procedure for constructing a function of α & β for a given i-th column. The data to be prepared is {α*, β*} calculated using equation (8) for samples No. 1 to No. 5. As shown in Fig. 7 [step 3], α* and β* were independently plotted against $Z_{eff,ref}$, and interpolated using a linear function.

$$\alpha(Z_{tent}):\ \text{Interpolation function of } \{Z_{eff,ref}, \alpha*\} \text{data for Nos. } 1-5 \tag{9-1}$$

$$\beta(Z_{tent}):\ \text{Interpolation function of } \{Z_{eff,ref}, \beta*\} \text{data for Nos. } 1-5 \tag{9-2}$$

For data falling outside the calibration range, we did not perform forced extrapolation and adopted the values from the most recent data points. Therefore, the functions of α & β with respect to Z_{tent} over the entire region are expressed as follows:

$$\alpha(Z_{tent}) = \begin{cases} \alpha(6.0) \text{ for } Z_{tent} < 6.0 \\ \alpha(Z_{tent}) \text{ for } 6.0 \le Z_{tent} \le 13.0 \\ \alpha(13.0) \text{ for } Z_{tent} > 13.0 \end{cases} \tag{10-1}$$

$$\beta(Z_{tent}) = \begin{cases} \beta(6.0) \text{ for } Z_{tent} < 6.0 \\ \beta(Z_{tent}) \text{ for } 6.0 \le Z_{tent} \le 13.0 \\ \beta(13.0) \text{ for } Z_{tent} > 13.0 \end{cases} \tag{10-2}$$

The function created in this way was then used for the actual correction. Namely, by replacing Z_{eff} with Z_{tent}, these functions become Z_{tent} functions and can therefore be used directly in the algorithm shown in Fig. 3. These calculations were performed using custom code written with Mathematica programming software (Wolfram Research, Illinois, USA). Parallel computing was performed using a 64-core workstation (Ryzen, Threadripper Pro 5995WX), and the calculation time required for determining $\alpha(Z_{tent})$ and $\beta(Z_{tent})$ was 60 h.

2.4. Demonstration using actual food samples

Measurements of food samples were also conducted to validate the methodology. Fig. 5 [b] shows a photograph of the sample. The food sample consisted of two sea breams, one chub mackerel, and one snow crab. As these samples were unprocessed frozen products, they contained internal organs and bones. They were placed on a polystyrene tray using plastic wrap that does not interfere with X-ray imaging. The samples were arranged with appropriate overlapping so that the entire assembly fit within a 30 cm square. As a result, we were able to create a situation in which various materials were superimposed at varying thicknesses. The imaging conditions followed those described in the former section.

3. Results and discussion

3.1. Generation of α&β functions

Fig. 8 illustrates the process of determining α & β for sample No. 1 at i = 1100. The graph shown on the left is an array plot of $Diff_Z$ and $Diff_{\rho t}$ within the ranges $0.90 \le \alpha \le 1.10$ and $0.90 \le \beta \le 1.10$. When the color is closer to yellow, the values of $Diff_Z$ and $Diff_{\rho t}$ become smaller, which indicates that they are closer to the correct values. Parameter combinations extracted as falling within the permissible range are enclosed in a thick border.

As shown in the upper-left part of Fig. 8, the similar values of $Diff_Z$ are distributed along a 45-degree line; this means that the acceptable range is also distributed along the line. The reason for this can be explained by the algorithm used to calculate Z_{eff} [6]. When calculating Z_{eff}, the physical quantity $(\mu t)_h/(\mu t)_l$ is computed and it is converted into Z_{eff}. This means that if the ratio of β to α yields the same value, the calculated Z_{eff} will also be the same. For example, this situation was expressed as $\{1.00 \times (\mu t)_h\}/\{1.00 \times (\mu t)_l\} = \{0.95 \times (\mu t)_h\}/\{0.95 \times$

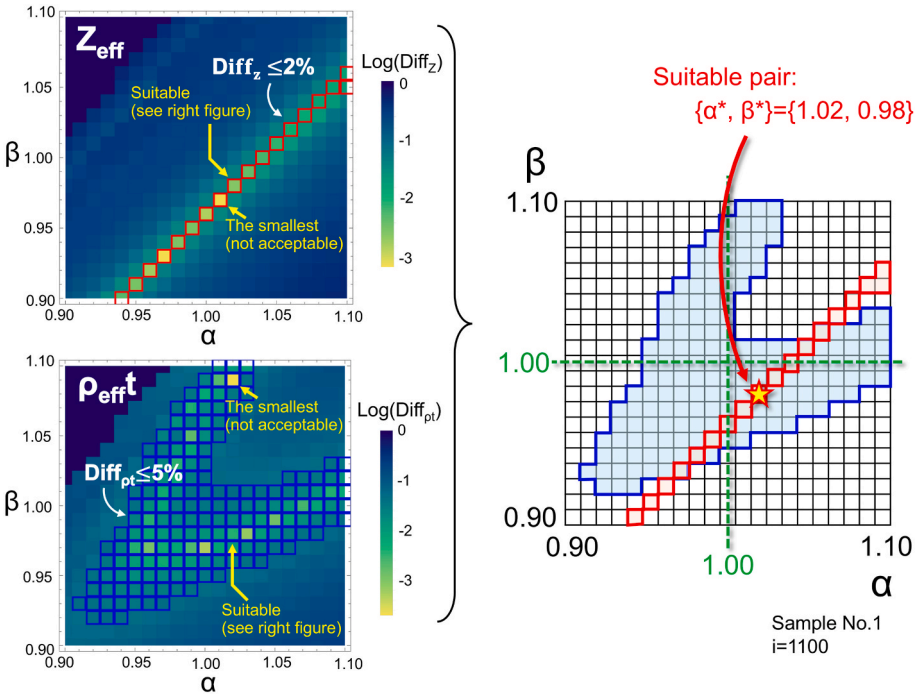

Fig. 8. Example of the process for determining a suitable pair of {α*, β*} under certain sample and certain i-th column condition.

$(\mu t)_l\}$. It should also be noted that the relationship becomes $(\mu t)_h/(\mu t)_l = (\mu/\rho)_h/(\mu/\rho)_l$ during this calculation process, meaning that the thickness information (t) is eliminated. Namely, if the suitable pair for α & β is calculated based solely on Z_{eff}, there is no guarantee that the effective mass thickness $\rho_{eff}t$ will be correct. Therefore, it was considered that the optimization process needs to take $Diff_{\rho t}$ into account.

In contrast, as shown in the bottom left of Fig. 8, the permissible

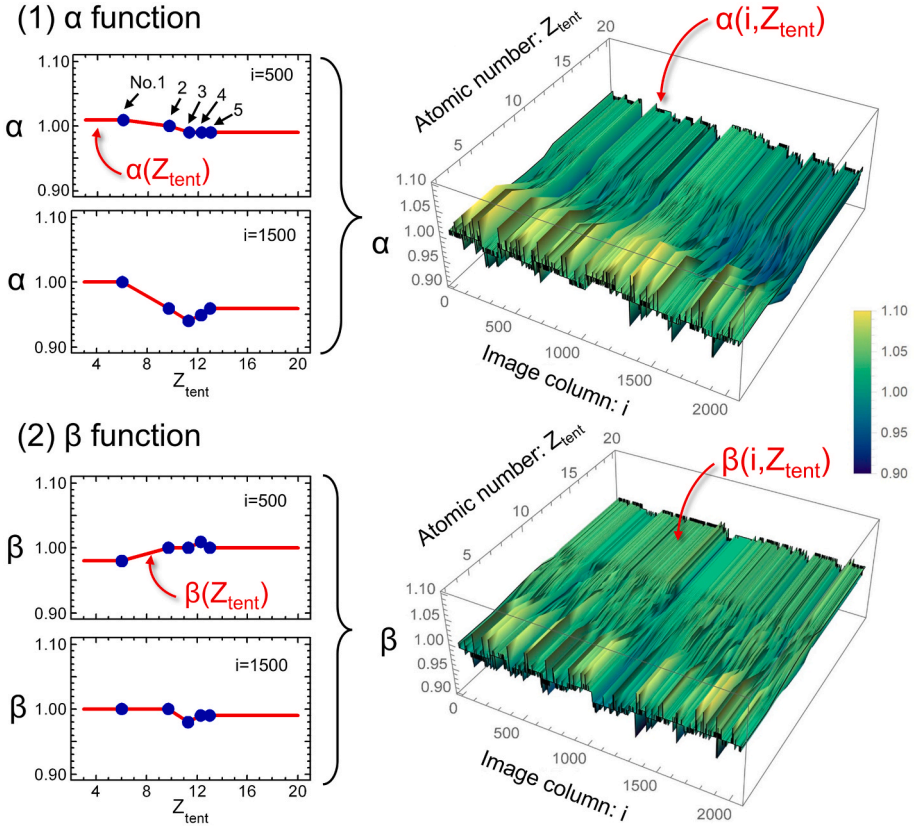

Fig. 9. Examples of calculating the α & β functions. By expressing these functions as three-dimensional functions taking the number of image columns (i) and Z_{tent} as arguments, they can be easily handled in programming code used to generate quantitative images.

range of $Diff_{\rho t}$ exhibits a horseshoe-shaped distribution, but the reason for this cannot be easily explained. This is because the calculation algorithm for $\rho_{eff}t$ involves a procedure of fitting the interaction cross-section (photon cross-section: σ), which is strongly influenced by Z_{eff}, to the X-ray attenuation values. In other words, the obtained $Diff_{\rho t}$ is significantly influenced by Z_{eff}.

The important point is that an overlap exists between the permissible range for $Diff_Z$ ($\leq$ 2%) and the permissible range for $Diff_{\rho t}$ ($\leq$ 5%). It should be noted that the suitable pair we are searching for is not the one consisting of the "minimum" values of $Diff_Z$ and $Diff_{\rho t}$. This is evident from the graph in Fig. 8; the minimum values of $Diff_Z$ and $Diff_{\rho t}$ correspond to clearly different {α, β} values, and no solution exists that completely satisfies the requirements for both. A key aspect of our algorithm lies in setting the permissible ranges in equations (7-1) and (7-2) to be relatively larger values. This is a crucial consideration for calculating the suitable pair {α*, β*}.

As shown on the right side of Fig. 8, there are multiple solutions for the permissible range of $Diff_Z$ and those of $Diff_{\rho t}$. Then, equation (8) was applied to these solutions, and the pair of {α, β} closest to {1, 1} was selected. In this case, the suitable pair was determined to be {α*, β*} = {1.02, 0.98}.

Fig. 9 shows the calculation results for the α & β functions. Fig. 9(1) shows an example of an α function. The graph shown on the left represents $\alpha(Z_{tent})$ for i = 500 and 1500. The 3D plot shown on the right represents α function for all columns, in which α was expressed as $\alpha(i, Z_{tent})$. It was observed that the α values show significant fluctuations from column to column. However, the magnitude of the fluctuation falls within the range of 0.95 to 1.05, indicating that it is approximately ±5%. Since quantitative image analysis is a highly precise analytical procedure, the presence of a correction factor of around 5% significantly affects image quality and cannot be ignored. It can be seen that most of these values are close to 1 when Z_{tent} is small, they drop when Z_{tent} is around 10, and recover to near 1 as Z_{tent} increases. These results demonstrate the importance of acquiring calibration data not only for C (Z = 6.0) and Al (Z = 13.0) but also for intermediate materials that are composed of combinations of these elements.

Fig. 9(2) shows an example of a β function. The graph shown on the left represents $\beta(Z_{tent})$, illustrating data for i = 500 and 1500. The graph shown on the right represents $\beta(i, Z_{tent})$. Overall, β values are distributed within the range of 0.95 to 1.05, and this trend is consistent with the results for α. If the initial settings for the defined energy bins (energy threshold values) are close to the correct values, it is expected that α & β will take values near 1. Conversely, if the initial energy bin settings differ significantly from the true values, a situation may arise in which the correct Z_{eff} cannot be calculated unless a large value is applied to α & β. In other words, by examining the overall trends of α & β, it is possible to derive information regarding the correctness of the initial settings for the energy bins.

A detailed examination of the data shown in Fig. 9 reveals that large correction coefficients are estimated at both ends of the sensor module. Although our imaging system applies a uniform response function to all pixels [24], parameters such as charge sharing may differ at the module edges. This phenomenon occurs because the α & β correction coefficients are used to force the characteristics of pixels with physically different parameters into the correct values. While we aim to simply correct these discrepancies using the α & β correction, the theoretically correct approach to minimizing the α & β correction coefficients is to apply appropriately estimated response functions for every position on the module. We plan to take this into account for the development of our imaging system.

3.2. Demonstration of corrected images

In this section, qualitative and quantitative evaluations of the uniformity were performed for the Z_{eff} and $\rho_{eff}t$ images obtained by applying the α & β functions.

Fig. 10 shows the results of calculating Z_{eff} and $\rho_{eff}t$ images for samples Nos. 1–5, as well as the results of profile analysis for the image of No. 5. Panel (a) shows the original image, in which our correction procedure was not applied. Significant variation is observed at the column level, and from a global perspective, there appear to be pronounced striped patterns associated with individual sensor units. Since each sensor unit has its own application specific integrated circuits (ASIC), in which configuration values such as energy bin widths (thresholds) are loaded, it is understandable that discrepancies arise between individual sensor units. However, since variations are observed between columns even within the same sensor unit, performing a column basis correction leads to the acquisition of high-quality data as proposed in this study. Panel (b) shows the corrected images. Image non-uniformity has been improved. The quantitative analysis results will be explained later.

In Z_{eff} images, uniform material exhibits a uniform value. For example, since No. 5 object is aluminum, the calculated Z_{eff} is 13 regardless of the column in the image. On the other hand, regarding $\rho_{eff}t$, it is necessary to consider the effect of X-ray incidence direction with oblique angle. When the incident angle of the X-rays is θ, the effective thickness of a material with thickness t is t/cosθ. In this study, the effect of oblique incidence was taken into account when calculating the difference in the $\rho_{eff}t$ image.

To quantify the effect of the correction, the average for each column of each image was calculated as shown in Fig. 10, and the root mean square error (RMSE) relative to the true value was calculated. Examining the profiles reveals that, while the original image exhibits significant variation across columns, the data in the proposed image are concentrated near the true values. This result indicates a substantial reduction in systematic uncertainty.

Fig. 11 shows the RMSE results for the Z_{eff} and $\rho_{eff}t$ images of Nos. 1–5. Fig. 11(A) shows the results for the Z_{eff} image, and Fig. 11(B) shows the results for the $\rho_{eff}t$ image. In these plots, the analysis results for the (a) original image and the (b) proposed image are compared. Focusing on the results for the Z_{eff} images, the RMSE was reduced by 78%–88%, which demonstrated a substantial reduction in non-uniformity. Focusing on the $\rho_{eff}t$ images, the RMSE was reduced by 18%–68%. For the Z_{eff} image, the uniformity of the original image was poor, and the target accuracy was strictly set at 2% as shown in equation (7-1); consequently, the values were corrected to be closer to the true values. On the other hand, the improvement effect for the $\rho_{eff}t$ image was smaller than that for the Z_{eff} image. This is because the accuracy of the original image was not particularly poor, and the target accuracy defined by equation (7-2) was set at a relatively lenient 5%. It is very interesting that the degree of improvement varies among the different bilayer samples, but analyzing them in detail is difficult. For example, in the corrected data for No. 1, low RMSE values (better results) are observed for both Z_{eff} and $\rho_{eff}t$; however, for No. 4, while Z_{eff} shows a relatively large RMSE, $\rho_{eff}t$ converges to a relatively low value.

Finally, we demonstrate the effect of the correction achieved by the proposed method using images of actual food samples. Fig. 12 shows the results. Panels (a) and (b) show the original and proposed images, respectively. The Z_{eff} image is shown in the upper panel, and the $\rho_{eff}t$ image in the lower panel. As indicated by the white arrows in the original image (a), non-uniform image artifacts are clearly visible for each sensor unit. Furthermore, we found that non-uniformity for each column was also observed within the sensor units themselves. Non-uniform image artifacts are observed particularly in Z_{eff} images. On the other hand, no noticeable artifacts are observed for the (b) proposed image, and the image appeared uniform.

In the example shown in Fig. 10, the methodology was demonstrated to function correctly for uniform samples for calibration, in which $\rho_{eff}t$ were ranging from 2.85 to 4.32 g/cm^2, but the robustness for the objects outside this range had not been verified. In the object shown in Fig. 12, along the center line, there are regions where fish and crab were overlapped. In this line, while $\rho_{eff}t$ is widely distributed, ranging from 0 to 8 g/cm^2, no significant artifacts are observed. These results demonstrate

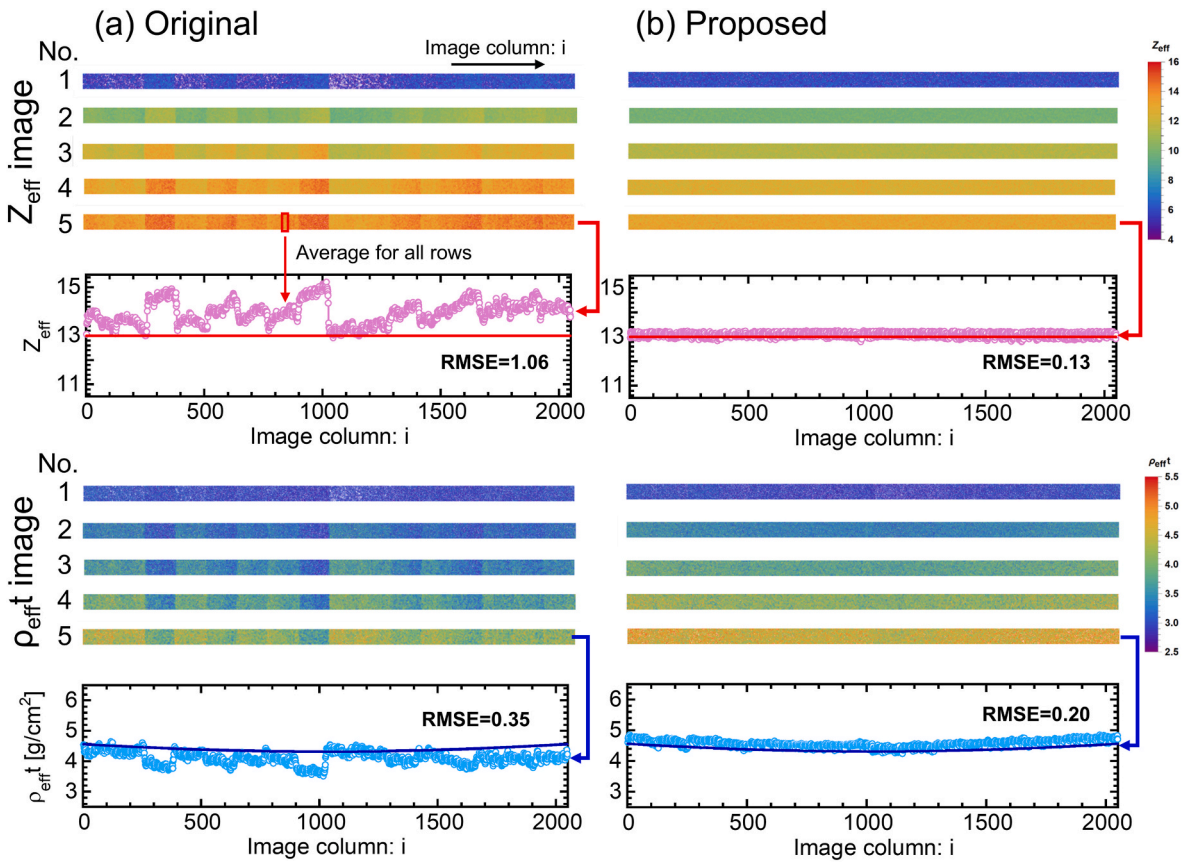

Fig. 10. Analysis results of the Z_{eff} and $\rho_{eff}t$ images (Nos. 1–5) and the profile of the No. 5 image. Panel (a) shows the original image obtained without using the proposed method, while panel (b) shows the result corrected for non-uniform image artifacts using the proposed procedure.

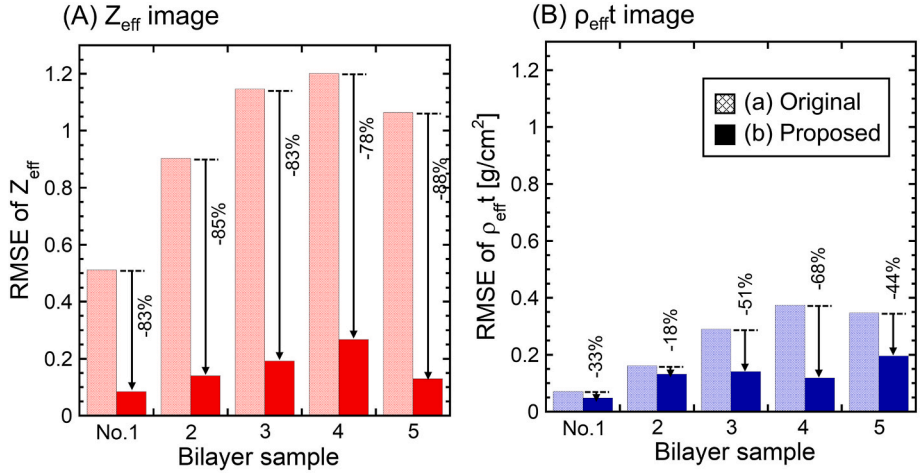

Fig. 11. RMSE analysis results for the profile curves of the bilayer samples. Panel (A) shows the results for the Z_{eff} image, and panel (B) shows the results for $\rho_{eff}t$. Each graph compares the results obtained using the (a) original data and (b) proposed image.

the practical applicability of the proposed method to substances encountered in non-destructive inspection in the food industry.

3.3. *Consideration for a correction factor dependent on Z_{eff}*

In this paper, we demonstrated that column-wise non-uniformity in quantitative X-ray images can be corrected by multiplying μt values by α & β. The most significant feature is that, instead of multiplying by constant α & β values, variables of α & β expressed as functions of Z_{eff} were used. When generating quantitative images using ERPCDs, the non-uniformity observed in the quantitative images stems from the failure to obtain accurate attenuation values for each energy bin. The primary cause of this is believed to be errors in setting the energy threshold values. However, even if the energy threshold values could be estimated with high precision, it is possible that the calculation precision might still be reduced by other factors. For example, response characteristics may vary from column to column, and such variations can adversely affect beam-hardening correction and response function correction for the attenuated data. The previously proposed quantitative image calculation algorithms are derived based on the calculation of Z_{eff}

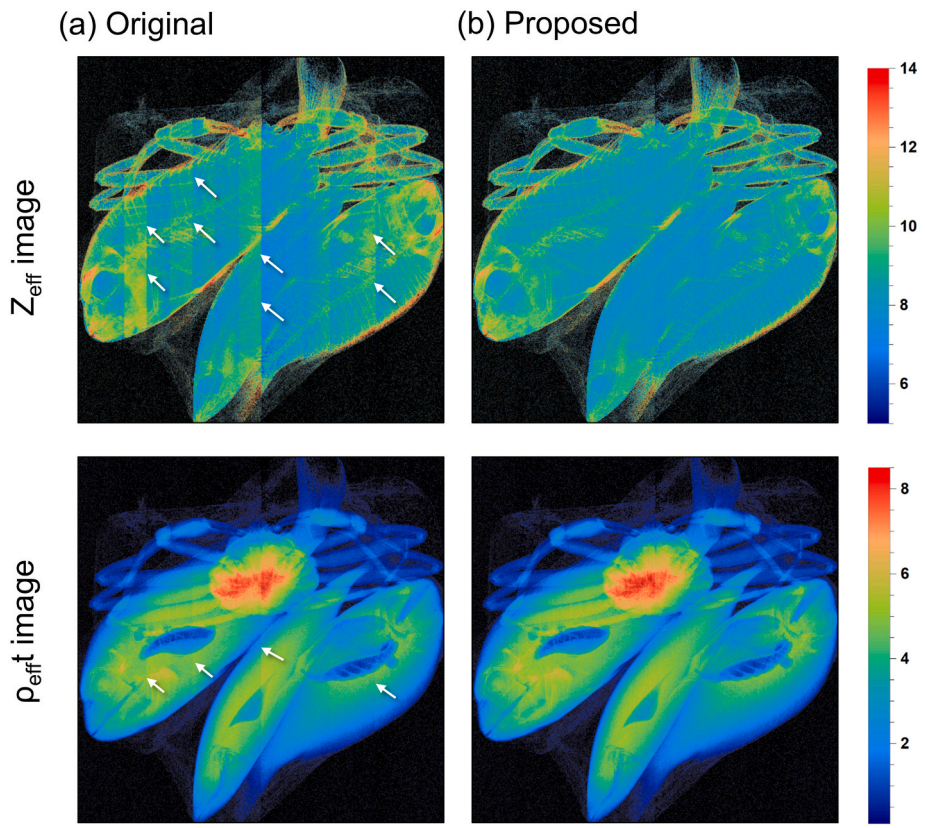

Fig. 12. Calculated Z_{eff} and $\rho_{eff}t$ images of the food sample. Panels (a) and (b) show the results for the original image and for the proposed image, respectively. The Z_{eff} and $\rho_{eff}t$ images show a slight depiction of the polystyrene tray used to hold the samples.

values [10,12,13]. In this context, by expressing α & β as functions of Z_{eff}, we can create correction coefficients that flexibly adjust to subjects with various Z_{eff} values. This approach makes the proposed correction procedure highly compatible with existing algorithms. In fact, as shown in Fig. 3, our α & β correction algorithm proposed in this paper could be incorporated into the existing algorithm.

To achieve more advanced correction, it would be necessary to develop an analysis algorithm that employs a correction factor incorporating information on $\rho_{eff}t$ in addition to Z_{eff}. However, it must be said that this attempt is extremely difficult. This is because, as shown in Fig. 3, the value obtained in the initial stage of analysis is the X-ray attenuation μt value. This physical quantity is the product of the mass attenuation coefficient (μ/ρ), which is related to Z_{eff}, and the mass thickness (ρt), and the two cannot be separated without advanced analysis of the X-ray attenuation. In our algorithm, we reduce the number of unknown variables by assuming the Z_{eff} value to be the Z_{tent} value, and perform BH correction while estimating parameters such as ρt. Since Z_{tent} thus serves as a fundamental factor within the algorithm, it is very convenient to treat α & β as variables dependent on Z_{tent}. On the other hand, for applications with limited scope such as measuring a known subject, defining correction factors for α & β as functions of ρt and developing a new algorithm could potentially enable higher-precision analysis.

Thus, the α & β correction algorithm proposed in this study is an empirical approach designed primarily for compatibility with existing Z_{eff} calculation algorithms, rather than a correction model derived directly from the underlying detector physics. Consequently, there remains room for further improvement.

3.4. Limitations

In this study, we evaluated the performance regarding the improvement of non-uniformity of quantitative image. The limitations of this study include the following. First, evaluations related to image visibility such as spatial resolution and blurring [30] have not been conducted and remain a task for future work. Improved image resolution has been reported as one of the features of ERPCDs [31,32], and therefore we intend to build upon our research to examine how the present correction procedure influences visibility. Next, since this study utilized only a single NDT system for the experiments, the general applicability of the proposed procedure cannot necessarily be verified. We plan to develop software that implements our methodology at short calculation time, for applying our procedure to various NDT devices to verify the robustness of the methodology.

4. Conclusion

In this study, we proposed a correction procedure for non-uniform image artifacts, which are caused by variations in detector settings and/or differences in detector response. We focused our attention on quantitative X-ray images, such as Z_{eff} and $\rho_{eff}t$ images, using a non-destructive inspection system equipped with an ERPCD. The proposed procedure applies different correction factors of α & β to the measured X-ray attenuation μt values for the low-energy and high-energy bins, respectively. A key feature of these α & β correction coefficients is that they are functions of the subject's Z_{eff}.

Demonstration experiments using non-destructive testing equipment showed RMSE reductions of 78%–88% for Z_{eff} images and 18%–68% for $\rho_{eff}t$ images. Furthermore, we imaged food samples having various mass thicknesses and Z_{eff} values, and demonstrated that similar improvement effects were achieved. In conclusion, we proposed a correction procedure for image non-uniformity that is crucial for the industrial application of non-destructive testing using quantitative X-ray images with ERPCDs.

CRediT authorship contribution statement

Hiroaki Hayashi: Writing – original draft, Project administration, Methodology, Investigation, Conceptualization. **Rina Nishigami:** Writing – review & editing, Methodology, Investigation, Formal analysis. **Daiki Kobayashi:** Software. **Takuya Kasue:** Writing – review & editing. **Mana Mitani:** Writing – review & editing. **Lisa Yakushiji:** Writing – review & editing. **Natsumi Kimoto:** Writing – review & editing, Visualization. **Takashi Asahara:** Writing – review & editing, Visualization.

Funding sources

This study was supported by Grants-in-Aid for Scientific Research [KAKENHI: 24K03306 (Hayashi), 25K21586 (Asahara), 25K21600 (Kimoto), 25KJ1355 (Kobayashi)].

Declaration of interests

The authors declare that they have no known competing financial interests or personal relationships that could have appeared to influence the work reported in this paper.

Acknowledgements

This paper was supported by funding reported in the funding source section. The phantoms used in this study was fabricated with the support of the Kanazawa University Technical Support Center. The authors would like to express their sincere gratitude to Mr. Hiroshi Saito and Mr. Takeshi Matsuoka for their invaluable assistance. The authors thank System Square Inc. for providing the experimental apparatus on loan for this study. The company had no role in the design of the study, data collection and analysis, decision to publish, or preparation of the manuscript.

References

[1] W. Sun, D.R. Symes, C.M. Brenner, M. Böhnel, S. Brown, M.N. Mavrogordato, I. Sinclair, M. Salamon, Review of high energy x-ray computed tomography for non-destructive dimensional metrology of large metallic advanced manufactured components, Rep. Prog. Phys. 85 (2022) 016102, https://doi.org/10.1088/1361-6633/ac43f6.

[2] D. Say, S.M. Qaisar, M. Krichen, S. Zidi, Artificial intelligence assisted non-destructive testing of welding joints: a review of techniques, X-ray image processing and applications, Eng. Appl. Artif. Intell. 160 (2025) 111792, https://doi.org/10.1016/j.engappai.2025.111792.

[3] X. Ou, X. Chen, X. Xu, L. Xie, X. Chen, Z. Hong, H. Bai, X. Liu, Q. Chen, L. Li, H. Yang, Recent development in X-Ray imaging technology: future and challenges, Research (2021) 9892152, https://doi.org/10.34133/2021/9892152.

[4] D. Pacella, Energy-resolved X-ray detectors: the future of diagnostic imaging, Rep. Med. Imag. 8 (2015) 1–13, https://doi.org/10.2147/RMI.S50045.

[5] J. van der Bie, M. van Straten, R. Booij, D. Bos, M.L. Dijkshoorn, A. Hirsch, S. P. Sharma, E.H.G. Oei, R.P.J. Budde, Photon-counting CT: review of initial clinical results, Eur. J. Radiol. 163 (2023) 110829, https://doi.org/10.1016/j.ejrad.2023.110829.

[6] N. Kimoto, H. Hayashi, T. Asakawa, C. Lee, T. Asahara, T. Maeda, S. Goto, Y. Kanazawa, A. Katsumata, S. Yamamoto, M. Okada, Effective atomic number image determination with an energy-resolving photon-counting detector using polychromatic X-ray attenuation by correcting for the beam hardening effect and detector response, Appl. Radiat. Isot. 170 (2021) 109617, https://doi.org/10.1016/j.apradiso.2021.109617.

[7] T. Asahara, M. Mitani, N. Kimoto, R. Nishigami, T. Kazuki, Y. Morimitsu, N. Akagi, T. Miyoshi, Y. Kanazawa, T. Iguchi, H. Hayashi, Applicability of effective atomic number (Z_{eff}) image analysis of coronary plaques measured with Photon- counting computed tomography, Investig. Radiol. 61 (2026) 378–386, https://doi.org/10.1097/RLI.0000000000001237.

[8] T. Asahara, S. Okada, H. Hayashi, T. Maeda, R. Nishigami, D. Kobayashi, C. Kurose, N. Kimoto, S. Goto, M. Hisatomi, Y. Yanagi, T. Iguchi, Helpfulness of effective atomic number image in forensic dental identification: Photon-counting computed tomography is suitable, Comput. Biol. Med. 184 (2025) 109333, https://doi.org/10.1016/j.compbiomed.2024.109333.

[9] M.G. Lima, E.I. Jussiani, X-ray computed tomography for effective atomic number and density evaluation: a review, Radiat. Phys. Chem. 225 (2024) 112130, https://doi.org/10.1016/j.radphyschem.2024.112130.

[10] H. Hayashi, R. Nishigami, T. Asahara, N. Kimoto, D. Kobayashi, M. Mitani, N. Akagi, F. Higaki, T. Iguchi, An algorithm to calculate physical density of biomedical objects having $3 \leq Z_{eff} \leq 20$: an application study using clinical photon-counting computed tomography equipment, Appl. Radiat. Isot. 236 (2026) 112768, https://doi.org/10.1016/j.apradiso.2026.112768.

[11] T. Asahara, R. Nishigami, N. Kimoto, M. Mitani, Y. Morimitsu, N. Akagi, F. Higaki, T. Iguchi, T. Hiraki, H. Hayashi, Potential of quantitative X-ray imaging from photon-counting CT: a novel analysis based on effective atomic number and physical density, J. Appl. Clin. Med. Phys. (2026) e70673, https://doi.org/10.1002/acm2.70673.

[12] R. Nishigami, N. Kimoto, T. Asahara, T. Maeda, D. Kobayashi, S. Goto, T. Haba, Y. Kanazawa, S. Yamamoto, H. Hayashi, Bone-enhanced high contrast X-ray images derived from attenuation estimation related to ultra-low energy X-rays – an application of an energy-resolving photon-counting detector (ERPCD), Radiat. Phys. Chem. 238 (2026) 113243, https://doi.org/10.1016/j.radphyschem.2025.113243.

[13] N. Kimoto, H. Hayashi, C. Lee, T. Maeda, M. Ando, Y. Kanazawa, A. Katsumata, S. Yamamoto, M. Okada, A novel algorithm for extracting soft-tissue and bone images measured using a photon-counting type X-ray imaging detector with the help of effective atomic number analysis, Appl. Radiat. Isot. 176 (2021) 109822, https://doi.org/10.1016/j.apradiso.2021.109822.

[14] A. Esquivel, A. Ferrero, A. Mileto, F. Baffour, K. Horst, P.S. Rajiah, A. Inoue, S. Leng, C. McCollough, J.G. Fletcher, Photon-Counting Detector CT: key points radiologists should know, Korean J. Radiol. 23 (2022) 854–865, https://doi.org/10.3348/kjr.2022.0377.

[15] C.H. McCollough, K. Rajendran, F.I. Baffour, F.E. Diehn, A. Ferrero, K. N. Glazebrook, K.K. Horst, T.F. Johnson, S. Leng, A. Mileto, P.S. Rajiah, B. Schmidt, L. Yu, T.G. Flohr, J.G. Fletcher, Clinical applications of photon counting detector CT, Eur. Radiol. 33 (2023) 5309–5320, https://doi.org/10.1007/s00330-023-09596-y.

[16] C.H. McCollough, K. Rajendran, S. Leng, L. Yu, J.G. Fletcher, K. Stierstorfer, T. G. Flohr, The technical development of photon-counting detector CT, Eur. Radiol. 33 (2023) 5321–5330, https://doi.org/10.1007/s00330-023-09545-9.

[17] J. Greffier, A. Viry, A. Robert, M. Khorsi, S. Si-Mohamed, Photon-counting CT systems: a technical review of current clinical possibilities, Diagn. Interventional Imaging 106 (2025) 53–59, https://doi.org/10.1016/j.diii.2024.09.002.

[18] D. Lee, X. Zhan, W.Y. Tai, W. Zbijewski, K. Taguchi, Improving model–data mismatch for photon-counting detector model using global and local model parameters, Med. Phys. 51 (2024) 964–977, https://doi.org/10.1002/mp.16883.

[19] D. Hein, K. Liappis, A. Eguizabal, M. Persson, Deep learning ring artifact correction in photon-counting spectral CT with perceptual loss. SPIE conference proceedings, 7th International Conference on Image Formation in X-Ray Computed Tomography, 123042Q (2022), https://doi.org/10.1117/12.2647089.

[20] E. Zhou, W. Li, W. Xu, Y. Lu, S. Chen, S. Wang, G. Zheng, T. Xie, Q. Liu, STEPC: a multi-energy nonuniform response calibration framework for photon-counting Micro-CT in multi-material imaging, IEEE Trans. Instrum. Meas. 75 (2026) 4006616, https://doi.org/10.1109/TIM.2026.3677968.

[21] D. Lee, X. Zhan, E.Y. Tai, W. Zbijewski, K. Taguchi, Pixel-to-pixel variation correction using cylindrical phantoms in photon-counting CT: total count results, SPIE Confer. Pro. 13405 (2025), https://doi.org/10.1117/12.3047221.

[22] S. Naidu, X. Jiang, W.Y. Tai, J. Wei, J.W. Stayman, W. Zbijewski, X. Zhan, K. Taguchi, Projection-domain material decomposition for PCD CT with pixel-to-pixel variations, in: SPIE Conference Proceedings, 13924, 2026, https://doi.org/10.1117/12.3086145.

[23] J.H. Hubbell, S.M. Seltzer, Tables of X-Ray Mass Attenuation Coefficients and Mass Energy-Absorption Coefficients 1 Kev to 20 Mev for Elements Z = 1 to 92 and 48 Additional Substances of Dosimetric Interest, 5632, NIST Publications, 1995.

[24] H. Hayashi, R. Nishigami, D. Kobayashi, T. Kasue, N. Kimoto, T. Asahara, Impact of correcting beam hardening and detector response function in photon-counting X-ray imaging when using anti-coincidence mode, Nucl. Eng. Technol. 59 (2027) 104678, https://doi.org/10.1016/j.net.2026.104678.

[25] R. Nishigami, D. Kobayashi, N. Kimoto, T. Asahara, T. Maeda, T. Haba, Y. Kanazawa, S. Yamamoto, H. Hayashi, Optimization of energy windows to calculate quantitative X-ray images using an energy-resolving photon-counting detector: a simulation study, Radiat. Phys. Chem. 229 (2025) 112460, https://doi.org/10.1016/j.radphyschem.2024.112460.

[26] N. Kimoto, R. Nishigami, T. Asahara, Y. Kanazawa, A. Katsumata, S. Yamamoto, H. Hayashi, Counting loss correction algorithm for an energy-resolving photon-counting detector for X-ray imaging of biological objects with effective atomic numbers between 3 and 20, Radiat. Phys. Chem. 243 (2026) 113723, https://doi.org/10.1016/j.radphyschem.2026.113723.

[27] N. Kimoto, R. Nishigami, D. Kobayashi, T. Maeda, T. Asahara, S. Goto, Y. Kanazawa, A. Katsumata, S. Yamamoto, H. Hayashi, Counting-loss correction procedure of X-ray imaging detectors with consideration for the effective atomic number of biological objects, Radiat. Phys. Chem. 239 (2026) 113237, https://doi.org/10.1016/j.radphyschem.2025.113237.

[28] Acrorad, Home page of Acrorad Co., Ltd. https://www.acrorad.co.jp/products/technology/basic.html. August 2026.

[29] S. Marupudi, J.A. Manus, M.U. Ghani, S.J. Glick, B. Ghammraoui, Evaluation of charge summing correction in CdTe-based photon-counting detectors for breast CT: performance metrics and image quality, J. Med. Imaging 12 (2025) 013501, https://doi.org/10.1117/1.jmi.12.1.013501.

[30] D. Kobayashi, H. Hayashi, R. Nishigami, T. Maeda, T. Asahara, Y. Kanazawa, A. Katsumata, N. Kimoto, S. Yamamoto, A blurring correction method suitable to analyze quantitative x-ray images derived from energy-resolving photon counting

detector, Phys. Med. Biol. (2024) 075023, https://doi.org/10.1088/1361-6560/ad3119.

[31] M. Remy-Jardin, A. Hutt, T. Flohr, J.-B. Faivre, P. Felloni, S. Khung, J. Remy, Ultra-High-Resolution photon-counting CT imaging of the chest: a new era for morphology and function, Investig. Radiol. 58 (7) (2023) 482–487, https://doi.org/10.1097/RLI.0000000000000968.

[32] P.C. Douek, S. Boccalini, E.H.G. Oei, D.P. Cormode, A. Pourmorteza, L. Boussel, S. A. Si-Mohamed, R.P.J. Budde, Clinical applications of photon-counting CT: a review of pioneer studies and a glimpse into the future, Radiology 309 (1) (2023) e222432, https://doi.org/10.1148/radiol.222432.